POLITECNICO DI TORINO
Repository ISTITUZIONALE

Effect of grain orientation and magnesium doping on -tricalcium phosphate resorption behavior

Original
Effect of grain orientation and magnesium doping on -tricalcium phosphate resorption behavior / Gallo, M.; Le Gars Santoni, B.; Douillard, T.; Zhang, F.; Gremillard, L.; Dolder, S.; Hofstetter, W.; Meille, S.; Bohner, M.; Chevalier, J.; Tadier, S.. - In: ACTA BIOMATERIALIA. - ISSN 1742-7061. - ELETTRONICO. - 89:(2019), pp. 391-402. [10.1016/j.actbio.2019.02.045]

Availability:
This version is available at: 11583/2959753 since: 2022-03-28T16:01:06Z

Publisher:
Acta Materialia Inc

Published
DOI:10.1016/j.actbio.2019.02.045

Terms of use:

This article is made available under terms and conditions as specified in the corresponding bibliographic description in the repository

Publisher copyright

(Article begins on next page)

20 July 2024

Acta Biomaterialia 89 (2019) 391–402

Contents lists available at ScienceDirect

Acta Biomaterialia

journal homepage: www.elsevier.com/locate/actabiomat

Full length article

Effect of grain orientation and magnesium doping on β-tricalcium phosphate resorption behavior

Marta Gallo [a,1], Bastien Le Gars Santoni [b,1], Thierry Douillard [a], Fei Zhang [a], Laurent Gremillard [a], Silvia Dolder [c], Willy Hofstetter [c], Sylvain Meille [a], Marc Bohner [b,2], Jérôme Chevalier [a], Solène Tadier [a,*]

[a] Univ Lyon, INSA Lyon, UCB Lyon 1, CNRS, MATEIS UMR 5510, Bât. Blaise Pascal, 7 Avenue Jean Capelle, 69621Villeurbanne, France
[b] RMS Foundation, Bischmattstrasse 12, 2544 Bettlach, Switzerland
[c] Department for BioMedical Research (DBMR), University of Bern, Murtenstrasse 35, 3008 Bern, Switzerland

ARTICLE INFO

Article history:
Received 19 July 2018
Received in revised form 5 February 2019
Accepted 27 February 2019
Available online 1 March 2019

Keywords:
Electron backscatter diffraction (EBSD)
Dissolution behavior
Osteoclastic resorption
Crystal orientation
Calcium phosphate

ABSTRACT

The efficiency of calcium phosphate (CaP) bone substitutes can be improved by tuning their resorption rate. The influence of both crystal orientation and ion doping on resorption is here investigated for beta-tricalcium phosphate (β-TCP). Non-doped and Mg-doped (1 and 6 mol%) sintered β-TCP samples were immersed in acidic solution (pH 4.4) to mimic the environmental conditions found underneath active osteoclasts. The surfaces of β-TCP samples were observed after acid-etching and compared to surfaces after osteoclastic resorption assays. β-TCP grains exhibited similar patterns with characteristic intra-crystalline pillars after acid-etching and after cell-mediated resorption. Electron BackScatter Diffraction analyses, coupled with Scanning Electron Microscopy, Inductively Coupled Plasma–Mass Spectrometry and X-Ray Diffraction, demonstrated the influence of both grain orientation and doping on the process and kinetics of resorption. Grains with *c*-axis nearly perpendicular to the surface were preferentially etched in non-doped β-TCP samples, whereas all grains with simple axis (*a*, *b* or *c*) nearly normal to the surface were etched in 6 mol% Mg-doped samples. In addition, both the dissolution rate and the percentage of etched surface were lower in Mg-doped specimens. Finally, the alignment direction of the intra-crystalline pillars was correlated with the preferential direction for dissolution.

Statement of significance

The present work focuses on the resorption behavior of calcium phosphate bioceramics. A simple and cost-effective alternative to osteoclast culture was implemented to identify which material features drive resorption. For the first time, it was demonstrated that crystal orientation, measured by Electron Backscatter Diffraction, is the discriminating factor between grains, which resorbed first, and grains, which resorbed slower. It also elucidated how resorption kinetics can be tuned by doping β-tricalcium phosphate with ions of interest. Doping with magnesium impacted lattice parameters. Therefore, the crystal orientations, which preferentially resorbed, changed, explaining the solubility decrease. These important findings pave the way for the design of optimized bone graft substitutes with tailored resorption kinetics.

© 2019 The Authors. Published by Elsevier Ltd on behalf of Acta Materialia Inc. This is an open access article under the CC BY-NC-ND license (http://creativecommons.org/licenses/by-nc-nd/4.0/).

1. Introduction

Calcium phosphate (CaP) materials are often used as bone substitutes thanks to their chemical composition similar to the one of the inorganic component of natural bones. These materials are intended to promote new bone formation and to be resorbed during time. It is generally admitted that their resorption kinetics should match that of bone growth to avoid a too early mechanical degradation and thus loosening of the interface between the substitute and the bone [1]. Although bio-resorption is a prerequisite for the effectiveness of the substitute, the resorption mechanisms are still far from being completely understood [2,3]. Thus, the study of the resorption behavior of CaP and the identification of the material parameters driving this process are essential in order to design optimized materials for bone substitution.

* Corresponding author.
E-mail address: solene.tadier@insa-lyon.fr (S. Tadier).
[1] Authors contributed equally to the work.
[2] Prof. Marc Bohner was an Editor of the journal during the review period of the article. To avoid a conflict of interest, Prof. William R. Wagner acted as Editor for this manuscript.

https://doi.org/10.1016/j.actbio.2019.02.045
1742-7061/© 2019 The Authors. Published by Elsevier Ltd on behalf of Acta Materialia Inc.
This is an open access article under the CC BY-NC-ND license (http://creativecommons.org/licenses/by-nc-nd/4.0/).

One approach is to study *in vitro* how osteoclasts (cells known to resorb bone tissue during the bone remodeling process) resorb CaP materials. These giant multinucleated cells adhere to the material surface creating a tight resorption area beneath them, where inorganic components of bones are resorbed via local acidification [2–5]. Indeed, protons released by osteoclasts locally lower the pH, leading to physico-chemical dissolution of calcium phosphate crystals. Thus, the characteristics of the material might affect both the osteoclast adhesion and activity and the solution-mediated dissolution in the acidic environment. Regarding the first aspect, it has been shown that material composition, solubility, grain size and crystallinity, as well as surface features (topography, roughness, pore size, wettability and surface energies) influence osteoclasts adhesion and resorption activity [3,6–11]. However, it has also been shown that not all the grains are equally dissolved within a resorbed area [8,12].

Seo *et al.* [13] highlighted by means of atomic force microscopy (AFM) that certain grains of dense hydroxyapatite were more prone to be dissolved than others when immersed in acidic conditions (pH = 3) used to mimic osteoclastic resorption. Possible reasons for this preferential dissolution behavior were suggested, such as variations in crystal orientation, surface energies and surface charges of exposed grains, but none of these hypotheses was assessed yet. Indeed, the relation between grain orientation and dissolution behavior of polycrystalline bioceramics is barely reported in the literature, probably because dissolution studies of CaP materials are generally performed on mineral powders rather than on bulk materials [14]. Smith *et al.* [15] reported that $CaCO_3$ calcite crystals with a specific initial crystallographic orientation (corresponding to the highest surface energies) are the most reactive. Therefore, they dissolve faster than the others and develop morphologies with lower energies. Consequently, the influence of the surface orientation of calcite grains on their dissolution kinetics appears to decrease with time, becoming negligible for long-term observations. Wang *et al.* [16,17] showed that demineralization of tooth enamel (>95 wt% CaP apatite) in acidic solution progresses anisotropically along the apatite crystals: the dissolution rate is higher in the direction perpendicular to their *c*-axis than in the parallel direction. However, the question of the influence of the grain orientation on the resorption behavior of CaP bulk materials used as bone graft substitutes remains open.

Among CaPs, beta-tricalcium phosphate ($Ca_3(PO_4)_2$, β-TCP) is used as a bone graft substitute in the form of granules or blocks, for non-load-bearing applications [18,19]. The β-polymorph of TCP, stable at room temperature, is preferred to the α-one (stable between 1180 °C and 1400 °C), because of its biocompatibility, its higher mechanical strength and its lower dissolution rate [20]. Actually, β-TCP is poorly soluble in physiological conditions, and it is therefore mainly resorbed by a cell-mediated process [19,21].

β-TCP lattice is rhombohedral (cell parameters: $a = b = 10.43$ Å, $c = 37.39$ Å, $\alpha = \beta = 90°$, $\gamma = 120°$, [22,23]). However, this structure is often altered by the addition of dopants. Indeed, several studies focused on the addition of ions [20,24–28], which could hinder, or at least shift to higher temperatures, the β- to α-transition, enabling the sintering of denser materials. Moreover, doping can also have an effect on the resorption process of a material due to the release of ions, which can trigger specific cellular responses. One of the most efficient dopants of β-TCP is magnesium. For example, Mg can shift the temperature of β- to α-transition from 1180 °C to 1500 °C [20,29]. In addition, Mg ions enable tuning the resorption behavior of β-TCP since their insertion in the lattice decreases the solubility of the β-TCP phase [1,22,30,31]. Furthermore, Mg stimulates osteoblast proliferation, thus enhancing bone formation [32–34].

In the present study, non-doped and Mg-doped (1 and 6 mol%) β-TCP samples are compared in terms of dissolution in *in vitro* conditions simulating those of cellular resorption, i.e., at acidic pH. Their behavior in acidic solutions is then compared to results obtained by osteoclastic resorption assays. The aim of this study is to answer the main question:

Is the resorption behavior of CaP materials merely linked to chemistry or are there physical parameters (grain size and orientation) involved?

In the present work, particular attention is paid to the possible correlation between grain orientation and preferential dissolution in β-TCP and on the influence of Mg-doping on this correlation.

2. Materials and methods

2.1. Powders synthesis

Both non-doped (pure) and Mg-doped β-TCP samples were processed. For the non-doped samples, it was necessary to synthesize pure CDHA (Calcium Deficient Hydroxyapatite) powder by precipitation in an aqueous media [35,36]. Briefly, a diammonium phosphate $(NH_4)_2HPO_4$ solution (Roth, Art n° 5596.1, Batch n° 026238654) was added at a constant rate of 4 mL/min into a calcium nitrate $Ca(NO_3)_2$ solution (Merck, Art n° 13477-34-4, Batch n° B1371623640-720). During the addition, the pH was maintained at a fixed value of 8.0 with a concentrated ammonia NH_4OH solution (Sigma-Aldrich, Art n° 338818, Batch n° SZBF3200V). The nominal amounts of the reagents were used in precise quantities in order to obtain a Ca/P molar ratio of 1.50. Once the titration was complete, the synthesis was left for ripening during 48 h at 30 °C. Subsequently, the synthesis was filtered and cleaned twice with 250 mL of ultrapure H_2O. Afterwards, the wet cake was dried in a convection oven at 70 °C and finally grinded manually until it passed through a 500μ m sieve. This CDHA powder was then converted into β-TCP by a subsequent thermal treatment at 850 °C for 1 h.

For Mg-doped samples, β-TCP powders were synthesized by solid-state reaction starting from dicalcium phosphate anhydrous ($CaHPO_4$, Calcium Phosphate GFS Chemicals, Art: 1548, purity $\geq$ 99.95%) and commercial hydroxyapatite powder ($Ca_5(PO_4)_3OH$, Budenheim Tricalcium Phosphate, Art: C5381). In the case of low Mg-doped powders, the only source of Mg was the Mg contained as an impurity in the reagent powders. In the case of high Mg-doped TCP, magnesium phosphate octahydrate ($Mg_3(PO4)_2{\cdot}8H_2O$, Fluka, Art: 63132, purity $\geq$ 97%) was used as an additional Mg source. The amounts of introduced reagents were computed so that the nominal (Ca + Mg)/P atomic ratio was kept equal to 1.5 (i.e., the usual Ca/P ratio in β-TCP). For the high Mg-doped powder, the amount of $Mg_3(PO_4)_2{\cdot}8H_2O$ was calculated so as to substitute 5.6% of total calcium by magnesium ions (i.e., to reach a Mg/(Ca + Mg) atomic ratio of 0.056). Further details of the synthesis protocol are provided in [27].

2.2. Characterization of powders

To determine their content in impurities, as-prepared powders were dissolved in HNO_3 (69% (w/w), ROTIPURAN® Supra, Art: HN50.1, Roth) and subsequently diluted (1:100) in a matrix solution made of ultrapure H_2O with 3% HNO_3, 2% HCl (35% (w/w), ROTIPURAN® Supra, Art: HN53.1, Roth) and 0.01% HF (47–51% (w/w), UPA™, Art: SS52, Romil). Inductively Coupled Plasma–Mass Spectrometry (ICP-MS; Agilent 7700x, Agilent Technologies) was used to quantify the content of Na, Sr, Mg and Fe in each powder. Specifically, ^{23}Na, ^{88}Sr and ^{24}Mg and ^{56}Fe were calibrated with a certified multi-element standard (71A, 10 ppm, Inorganic Ventures) and successively diluted to 100, 10, 1 and 0.1 ppb. Measurement of an internal standard (1 ppb In, 1 ppb Sc and 0.1 ppb Bi,

Inorganic Ventures) allowed to compensate for calibration drifts over time. Measurements uncertainties ($U_{k=2}$) were determined for each element taking into account errors involving pipettes, sample weighing and instrument fluctuations over time.

2.3. Fabrication and sintering of dense samples

To obtain bulk specimens, two different approaches were used for non-doped and Mg-doped β-TCP samples. Pure and dense β-TCP cylinders were produced with the slip casting approach [36]. First, the specific surface area of the particles was reduced below 10 m^2/g by a thermal treatment at 850 °C for 1 h. The agglomerates formed during the previous thermal treatment were destroyed by ball-milling for 2 h (medium: ultrapure H_2O). The powder was then dried at 70 °C overnight to remove residual H_2O. Finally, in ultrapure H_2O, a slurry (65 wt% of powder) was made using Darvan C-N (R.T. Vanderbilt Co, Norwalk, CT USA) as a dispersant, in amount 1.0 wt% of the powder content. To ensure a good homogenization of the slurry, 30 min grinding in a ball mill was done. After this mixing step, 200 μL of the slurry were pipetted into a mould (96 polystyrene well-plate cut at both side) already placed on a gypsum block. After 12 h of drying (22 °C, 40% RH), green bodies were demoulded and sintered at 1100 °C for 3 h on a zirconia (ZrO_2) plate. After sintering, the mean diameter of the non-doped β-TCP cylinders was 5.48 ± 0.03 mm (n = 4 cylinders). For Mg-doped β-TCP, the powders (previously milled with 10 wt% of fumaric acid and ethanol as described in [27]) were placed in a cylindrical die (Φ = 10 mm) and pressed at room temperature, first uniaxially at 130 MPa for 45 s, and then isostatically at 400 MPa for 40 s. The so-obtained disks were sintered at 1100 °C for 20 h (with a dwell at 800 °C for 1 h to eliminate all traces of fumaric acid). After sintering, the mean diameters of low Mg-doped and high Mg-doped β-TCP cylinders were 8.26 ± 0.05 mm (n = 20 cylinders) and 8.41 ± 0.03 mm (n = 20 cylinders), respectively.

Apparent densities of sintered disks were computed considering that all types of samples were composed of 100% β-TCP (density of 3.07 g/cm^3). Then, samples were polished by conventional diamond polishing down to 1 μm completed by vibratory polishing with colloidal silica (0.1 μm).

2.4. Etching in acidic solution

To simulate the environment at the surface of an implanted material during cellular resorption, each sample was immersed in 200 mL of an aqueous solution of pH 4.4 composed of HCl (Fisher Chemical) and $NaHCO_3$ (1.4 $mol.L^{-1}$, Sigma Aldrich, purity: 99.5–100.5%). Different immersion durations were tested: 5 min, 15 min, 30 min, 1 h, and until 5 h for samples with the highest Mg content. Once removed from the acidic solutions, samples were rinsed thoroughly with deionized water and then dried at 100 °C. After characterization at a specific etching time, some samples were re-immersed in their own solution to allow more time for acid-etching and to monitor their evolution.

2.5. Osteoclasts differentiation and cell-mediated resorption assays

Osteoclast resorption assays were conducted to compare the dissolution of β-TCP samples in acidic conditions to cellular resorption. Bone marrow cells (BMC) were collected from femora and tibiae of 6 weeks old *C57Bl/6J* mice [37–39] by flushing them out with Hanks Balanced Salt Solution (HBSS, Sigma) supplemented with 1% penicillin/streptomycin (P/S, GIBCO) [38,40]. Cells were sedimented and re-suspended in cell culture medium composed of α-minimum essential media (α-MEM, GIBCO) with 10% fetal bovine serum (FBS, Sigma), 1% P/S and 30 ng/mL macrophage colony-stimulating factor (M-CSF, Chiron) [37,38]. A total amount of around 42×10^6 BMC was seeded into a 75 cm^2 culture flask and incubated (37 °C in a humidified atmosphere with 5% CO_2) [37,38]. After 24 h, the non-adherent M-CSF dependent osteoclast progenitor cells (OPC) were collected, centrifuged (7 min, 1200 rpm, 4 °C) and dispersed in cell culture medium, containing receptor activator of nuclear factor κ-B ligand (recombinant human RANKL, PeproTech) at a density of 4×10^5 cells/mL [37]. OPC were cultured in two Petri dishes (20 cm^2/dish) and differentiated into osteoclasts within 5 days [37,38,41,42]. For the assessment of resorption, non-doped and Mg-doped β-TCP sintered cylinders (polished and unpolished, respectively) were sterilized by dry heat (180 °C for 6 h). These β-TCP cylinders were placed into a 96-well plate, coated with 150 μL of cell culture medium containing 30% of FBS per well and incubated for 48 h (37 °C, humidified atmosphere, 5% CO_2) [37,41]. This coating medium, removed after incubation, enabled to saturate the protein binding sites of the material and allowed for better cell adhesion and survival. At day 5, mature osteoclasts were dissociated from the Petri dishes by incubating them at 37 °C for 10 min in Dulbecco's Phosphate-Buffered Saline (PBS, pH 7.4; Sigma-Aldrich) with 0.02% ethylenediaminetetraacetic acid (EDTA, Merck) [38]. Osteoclasts were re-suspended in 416 μL of cell culture medium per dish. 25 μL of the cell suspension were distributed on each β-TCP cylinder [37,39], (supplementary data, Fig. S1). To each well, 125 μL of medium supplemented with M-CSF (30 ng/ml), HCl (15 mM) and RANKL (5 or 20 ng/mL) were added. Cells were left for 24 h in contact with the samples for resorption.

2.6. Characterization of samples

Samples were characterized before and after acid-etching and cell-mediated resorption. X-Ray Diffraction (XRD) analyses were performed using a D8-Advance diffractometer (Bruker, Germany) with a Lynx-Eye Position Sensitive Detector, using Cu Kα radiation, from 10° to 90° (2θ) with a 0.03° (2θ) step size and 2.4 s/step counting time. The obtained diffractograms were analyzed using the EVA software (Bruker) and phases were identified by comparing the peaks present to PDF files (mainly, files #09-0432 for hydroxyapatite, 09-0348 for α-TCP and 09-0169 for β-TCP). The data were further exploited by Rietveld refinements using the Topas 4 software (Bruker), with a fundamental parameters approach and refining only the scale factor, lattice parameters, crystallite size (parameter *Cry Size L*) and strain (parameter *Strain G*).

A fundamental part of the characterization was performed by Scanning Electron Microscopy (SEM) and Electron BackScatter Diffraction (EBSD). SEM images and EBSD maps were obtained with a Zeiss Supra 55VP SEM (Carl Zeiss Microscopy GmbH, Oberkochen, Germany) equipped with a Gemini I SEM column. β-TCP being an insulating material, a low vacuum configuration (10 Pa of gaseous nitrogen) was adopted, in order to avoid any deleterious charge effect without needing to carbon-coat the samples. For EBSD maps, the accelerating voltage was set to 10 kV, samples were tilted to the standard 70° angle and the objective lens aperture was of 120 μm. The so-called High Current Mode was activated and an optimum working distance of 12 mm with respect to the pattern center was used. EBSD maps were acquired with a Nordlys S camera and data were post-processed with HKL Channel5 software (Oxford Instruments, Abingdon, UK), to suppress the non-indexed points without affecting the orientation of their neighbors. EBSD mapping was performed on etched samples, on an area 74 μm × 56 μm (ca. 600 grains). Samples were sensitive to a long electron irradiation (the exposure time per point was around 45 ms for EBSD acquisitions): areas already mapped before acid-etching dissolved to a different extent compared to non-mapped zones. As a consequence, since the etched grains diffracted

enough signal to be indexed (indexing rate of the overall map typically equal to 75%), EBSD maps analyzed in this work were acquired directly after etching. The rhombohedral β-structure used for indexing is given in [23]. SEM images were obtained at low accelerating voltage (1 kV) with secondary electrons and at 10 kV with backscattered electrons for a better assessment of the etched grains. They were then analyzed by means of the public domain Java-based ImageJ/Fiji shareware [43], in order to quantify the percentage of etched grains. Since any automatic procedure (i.e., automatic filters and threshold) was unsuitable for discriminating the etched grains from non-etched ones, a manual procedure was preferred. In details, etched grains were manually identified in the images; afterwards, the images were binarized so that the etched grains appeared in black and all the others in white. Finally, the software automatically calculated the percentage of black surface (i.e., of etched grains). This procedure was performed by three different operators on micrographs showing around 600 grains for each immersion duration; the percentage of etched surface reported in the following is given as a mean value ± standard deviation. The grain sizes were quantified using EBSD maps and SEM images according to the linear intercept method. Measurements were performed using the overlays of EBSD maps and SEM images, enabling clear discrimination of the etched vs. non-etched grains.

2.7. Statistical analysis

Experimental data on ICP-MS titrations (Table 1) are expressed as mean ± $U_{k=2}$. Percentages of etched surfaces were computed by three different operators. They are plotted (Fig. 1b) as mean value ± standard deviation. Mean grain sizes are given in Table 3 as follows: mean value ± 95% confidence interval. The significance of differences in the mean and median values were analyzed by T-test and Mann-Whitney Test (significance level $\alpha = 0.05$), respectively.

3. Results

Magnesium, sodium, strontium and iron contents of non-doped and Mg-doped powders are reported in Table 1. Pure β-TCP powder was obtained from ultra-pure raw materials, synthesized in the lab. It contained trace amounts of strontium, but contents in magnesium, sodium and iron remained below the limits of detection or quantification of these elements. Although no Mg was intentionally added in the second β-TCP powder (named low Mg-doped in Table 1), ICP-MS titrations showed that it contained a considerable amount of Mg (2300 ppm). Thus, samples prepared from this powder will be referred to as "low Mg-doped" samples. The third β-TCP powder (high Mg-doped, for which magnesium phosphate octahydrate was intentionally added during the synthesis) contained around 13000 ppm Mg (Table 1), i.e. about 5.7 times more magnesium than the low Mg-doped powder. Both Mg-doped powders also included similar amounts of Na, Sr and Fe (Table 1).

After sintering, the apparent porosities of the small cylinders obtained were: 1.2 ± 0.1% for pure β-TCP, 7.8 ± 0.8% for low Mg-doped β-TCP and 8.1 ± 0.9% for high Mg-doped samples. Rietveld refinements showed that both non-doped and high Mg-doped samples were made of 100% β-TCP (Table 2), while the low Mg-doped samples contained around 4.7 wt% of hydroxyapatite (HA). Lattice parameters of the β-TCP phase, also calculated by Rietveld refinements, decreased with increasing Mg content (Table 2).

The grains of pure β-TCP were slightly larger than the grains of both types of Mg-doped samples (Table 3). Comparing low and high Mg-doped samples, the same size distributions and similar average and median values ($P < 0.05$) were computed (Table 3), as also displayed in the SEM images of both Mg-doped samples, once polished (Fig. 1a).

The effect of immersion duration of these samples in the acidic solution is illustrated in Fig. 1. In terms of dissolution, grain boundaries were sensitive to the acidic environment and dissolved quickly (already at 5 min). However, the dissolution of the grains themselves was assessable in low Mg-doped samples after 5 min but hardly detectable in high Mg-doped β-TCP before 30 min of immersion (Fig. 1a, b). Fig. 1a shows the same zone of each type of sample before and after immersion in acidic solution, for 30 min and 1 h. No matter the composition, once the grains had started to dissolve, they were etched deeper with increased immersion time, resulting in a rougher surface (Fig. 1a). For low Mg-doped β-TCP, the percentage of etched surface increased rapidly and up to 15 min of immersion. Then, it remained nearly constant, around 38% (Fig. 1b) and the grains unaltered after 30 min appeared still intact after 1 h etching (Fig. 1a). On the contrary, the etched surface area of high Mg-doped samples kept on increasing up to 39% after 5 h, reaching a percentage of etched surface equivalent to the one obtained in low Mg-doped β-TCP after only 15 min (Fig. 1b).

Comparing the three different compositions of β-TCP after 1 h etching, the percentage of etched surface significantly decreased when the content in Mg increased (Fig. 2a). It reached around 54% for non-doped β-TCP, 40% for low Mg-doped and 20% for high Mg-doped samples. In all cases, an extensive dissolution of the grain boundaries and a partial resorption of TCP grains were observed (Fig. 2a). In non-doped and low Mg-doped samples, whereas some of the grains seemed to be undamaged, the etched ones showed distinct features of multiple unidirectional spike-like intra-crystalline structures (Fig. 2a). After the same etching duration in the acidic solution (1 h), a similar tendency was observed for high Mg-doped samples but to a lower extent (lower roughness and no characteristic spike-like sub-crystals, Fig. 2a).

SEM images of β-TCP samples in contact with osteoclasts for 24 h also display heterogeneously resorbed surfaces. Topological observations are very similar to those already depicted for acid-etched samples (Fig. 2): extensive dissolution of the grain boundaries is experienced for all samples and cell mediated resorption considerably decreases with increasing Mg-doping. High Mg-doped β-TCP samples do not seem to exhibit any noticeable difference among grains. On the contrary, for non-doped samples, some areas were left completely un-resorbed (supplementary data, Fig. S2-b: such areas are highlighted by dots), while osteoclasts

Table 1
Content in magnesium and other trace elements of the three β-TCP powders (non-doped and Mg-doped), as-titrated by ICP-MS measurements (n = 2).

β-TCP powders	^{24}Mg Concentration [mg/kg]	^{23}Na concentration [mg/kg]	^{88}Sr concentration [mg/kg]	^{56}Fe concentration [mg/kg]
Pure β-TCP	<6**	<LOD*** (LOD = 57)	19 ± 4*	<14**
Low Mg-doped	2344 ± 223*	309 ± 113*	164 ± 15*	124 ± 10*
High Mg-doped	13419 ± 1275*	302 ± 109*	159 ± 15*	107 ± 9*

* $U_{k=2}$ from validation.
** Limit of Quantification.
*** LOD = Limit of Detection.

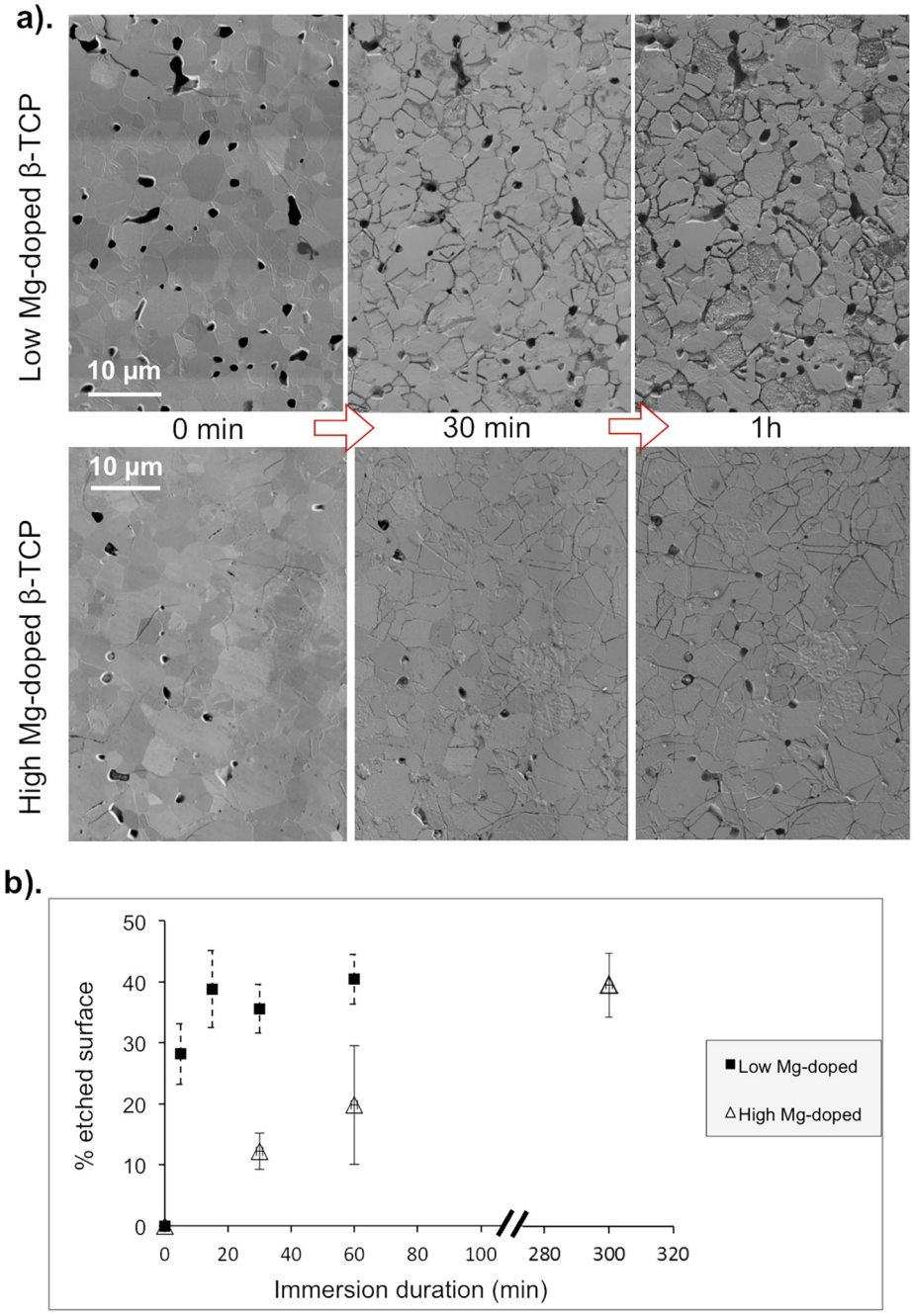

Fig. 1. a). SEM images of low Mg-doped and high Mg-doped β-TCP samples as–prepared ("0 min") and immersed for different durations in acidic solution; b) percentage of etched surface versus immersion time in acidic solution. In high-Mg-doped samples, etched and non-etched grains can hardly be discriminated before 30 min.

trails and extensively resorbed areas could be morphologically identified (supplementary data, Fig. S2-b: such areas are pointed out by arrows). Such a resorbed area, in which all grains were etched, is illustrated in Fig. 2b. The characteristic resorption pattern with multiple intra-crystalline pillars is exposed, showing that, within each grain, pillars are all aligned along the same direction (Fig. 2b).

To clarify why, regardless of the Mg-content, the immersion in the acidic solution etched some grains and left others intact (Fig. 2a), the features of etched and non-etched grains were compared. In particular, grain size distribution and mean grain size (Table 3) were analyzed. Although not significant ($P < 0.05$), a small difference was constantly noted in the grain sizes between non-etched and etched grains: in pure β-TCP, etched grains were slightly smaller than non-etched grains, whereas the contrary was noted for Mg-doped samples (Table 3). Similarly, Rietveld refinements showed few changes between initial and acid-etched samples. Looking at the overall composition, a slight decrease of the quantity of HA detected in low Mg-doped samples was measured (Table 2). Besides, whereas the lattice parameter along the *c*-axis decreased slightly (but significantly) after the immersion in acidic solution, it seemed that the other lattice parameter tended to increase (Table 2).

Finally, Rietveld refinements did not evidence any texture at the surface of β-TCP samples: no preferred crystal orientation was identified, neither before nor after acid-etching. Thus, over a representative surface, grains were randomly oriented, as later confirmed by EBSD acquisitions.

Table 2
Composition and lattice parameters of bulk samples before and after immersion in acidic solution (1 h etching for the non-doped sample and the low Mg-doped one and 5 h etching for the high Mg-doped one), computed from Rietveld refinements.

	Sintered β-TCP samples	Phase composition (wt.%)	Lattice parameters of the β-TCP phase (this work)	
			a = *b* (Å)	*c* (Å)
Before acid-etching	**Pure β-TCP** (non-doped)	β-TCP: 100	10.427 ± 0.001	37.451 ± 0.002
	Low Mg-doped (≈1 mol%)	β-TCP: 95.3 ± 0.4 HA: 4.7 ± 0.4	10.423 ± 0.001	37.387 ± 0.001
	High Mg-doped (≈6 mol%)	β-TCP: 100	10.376 ± 0.001	37.250 ± 0.001
After acid-etching	**Pure β-TCP** (1 h)	β-TCP: 100	10.432 ± 0.001	37.447 ± 0.002
	Low Mg-doped (1 h)	β-TCP: 96.3 ± 0.3 HA: 3.7 ± 0.3	10.425 ± 0.001	37.374 ± 0.001
	High Mg-doped (5 h)	β-TCP: 100	10.379 ± 0.001	37.246 ± 0.005

Table 3
Mean grain sizes of samples before and after immersion in acidic solution. Measurements were performed on EBSD maps, before etching and after 1 h and 5 h etching. In the latter cases, grain sizes of both etched and non-etched grains are reported (±95% confidence interval).

Sintered β-TCP samples	Before etching (μm)	After 1 h etching		After 5 h etching	
		Non-etched grains (μm)	Etched grains (μm)	Non-etched grains (μm)	Etched grains (μm)
Pure β-TCP	2.75 ± 0.11	2.99 ± 0.25	2.88 ± 0.36	/	/
Low Mg-doped	2.54 ± 0.15	2.40 ± 0.22	2.67 ± 0.35	/	/
High Mg-doped	2.60 ± 0.10	2.41 ± 0.32	2.75 ± 0.36	2.54 ± 0.34	2.73 ± 0.30

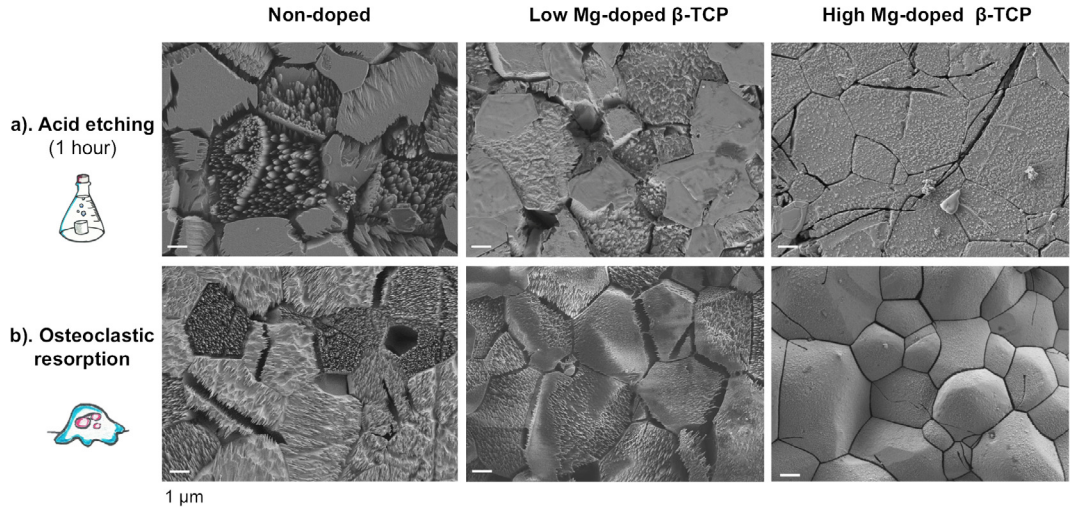

Fig. 2. SEM images of the surfaces of non-doped and Mg-doped β-TCP samples: a). after 1 h immersion in the acidic solution (above) and b). after 24 h of contact with osteoclast cells (RANKL concentration = 20 ng/mL, below). Scale bar = 1 μm for all micrographs.

EBSD maps performed at the surface of pure β-TCP acid-etched for 1 h do not reveal any specific orientation of the grains that were preferentially etched (Fig. 3a). However, the still intact grains were all oriented with *c*-axis parallel to the surface (Fig. 3b).

For low Mg-doped samples, after 1 h in acidic solution, β-TCP grains with *c*-axis [0 0 0 1] nearly normal to the surface were preferentially etched (Fig. 4a): two examples of such crystal orientations are sketched on top of Fig. 4a. Surprisingly, some of these grains were only partially etched. However, the other grains, again oriented with *c*-axis parallel to the surface, remained completely intact (Fig. 4b).

High Mg-doped samples were less etched than non-doped and low Mg-doped ones after 1 h immersion (see supplementary data, Fig. S3), consistently with what was previously observed by SEM (Figs. 1 and 2). Thus, to discriminate more clearly between etched and intact grains, without risking any overestimation, high Mg-doped samples were immersed for 4 additional hours in the acidic solution (Fig. 5). After 5 h immersion, almost all grains with simple axis (*a*, *b* or *c*) "nearly" normal to the surface were etched, as clearly testified by the inverse pole figure shown in Fig. 5a.

Finally, EBSD mapping was also performed at the surface of pure β-TCP after 24 h of cell-mediated resorption (Fig. 6). In the extensively resorbed regions, all grains were attacked, whatever their crystallographic orientation (Fig. 6). Fig. 7 illustrates the correlation of the crystallographic directions of the exposed grains with the direction of intra-crystalline pillars formed during immersion in the acidic solution (Fig. 7a) or during cell-mediated resorption (Fig. 7b). In both cases, when the *c*-axis of a grain (Miller index [0 0 0 1]) was nearly normal to the surface, close to the *Z* direction, the intra-grain pillars were also aligned perpendicularly to the surface. Consistently, in other grains, both the pillars and the *c*-axis tended to be parallel to the sample surface (Fig. 7).

4. Discussion

Although specific care was taken in the synthesis of low and high Mg-doped powders, ICP-MS measurements revealed that they

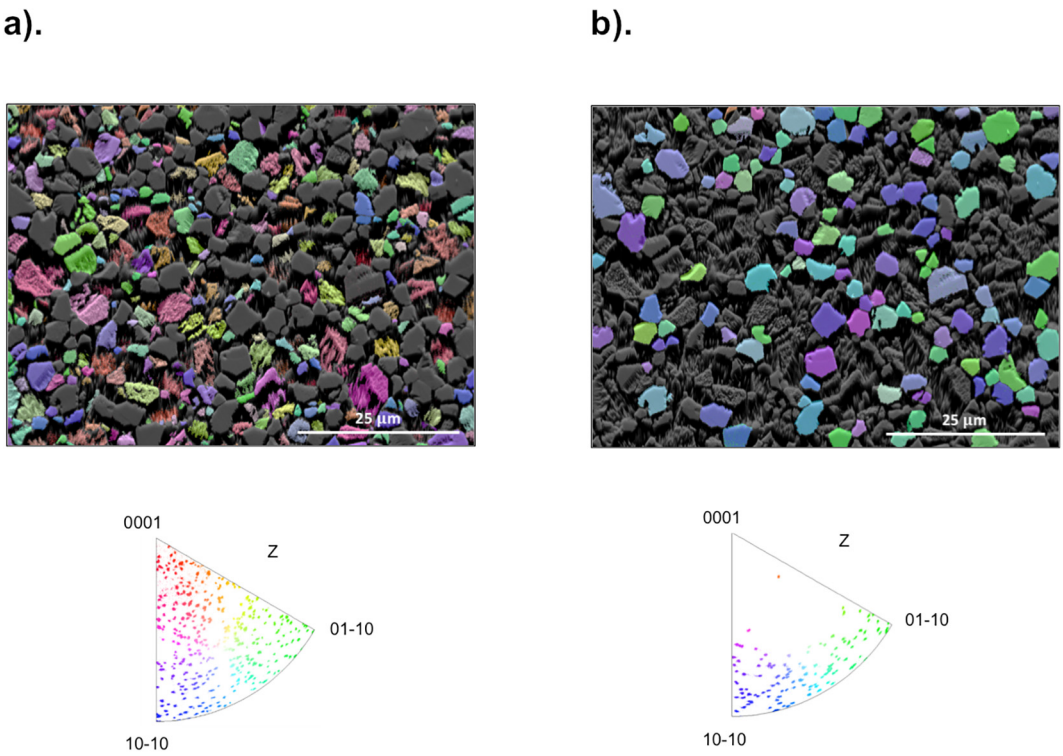

Fig. 3. Pure β-TCP acid-etched for 1 h: overlay of SEM images and crystal orientation maps derived from EBSD and displayed in Inverse Pole Figure (IPF) coloring (the reference direction is Z, i.e. the normal direction to the map): (a) etched grains and corresponding IPF (b) non-etched grains and corresponding IPF.

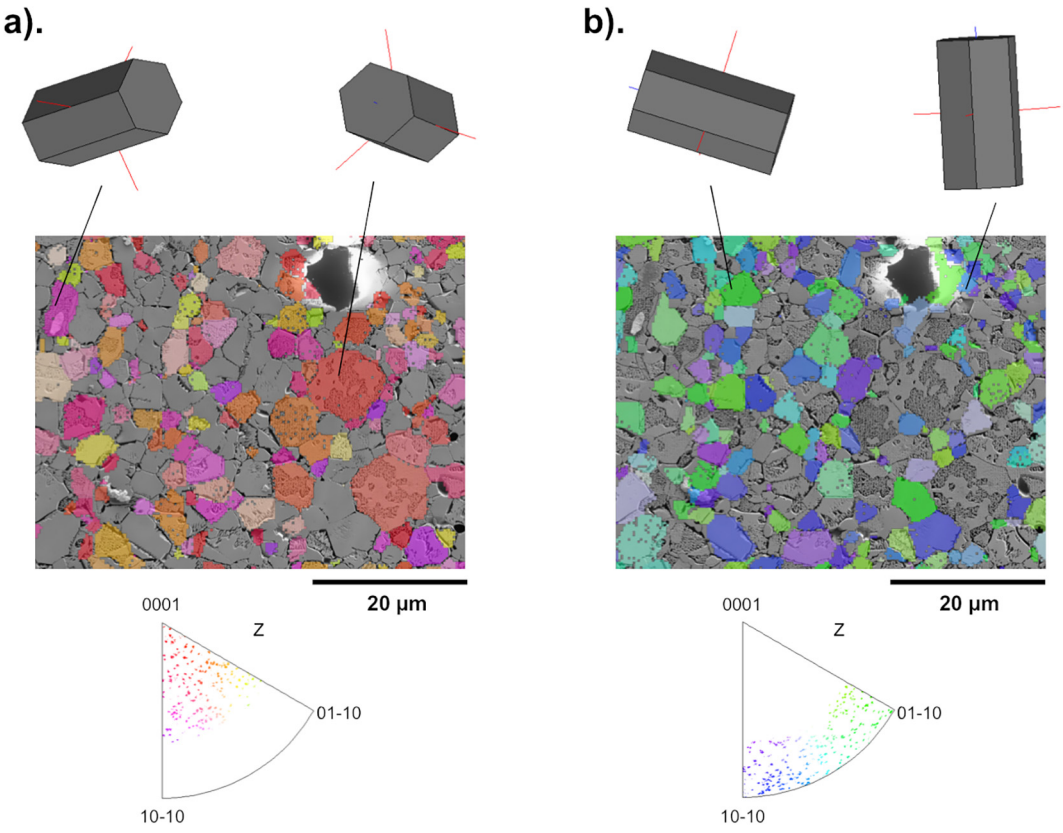

Fig. 4. Low Mg-doped β-TCP acid-etched for 1 h: overlay of SEM images and crystal orientation maps derived from EBSD and displayed in Inverse Pole Figure (IPF) coloring (the reference direction is Z, i.e. the normal direction to the map): (a) etched grains and corresponding IPF (b) non-etched grains and corresponding IPF. For both (a) and (b), examples of related 3D crystal orientation for two grains are shown on top of the figure. For Miller-Bravais indices of the 3D crystal representations, refer to Fig. 7.

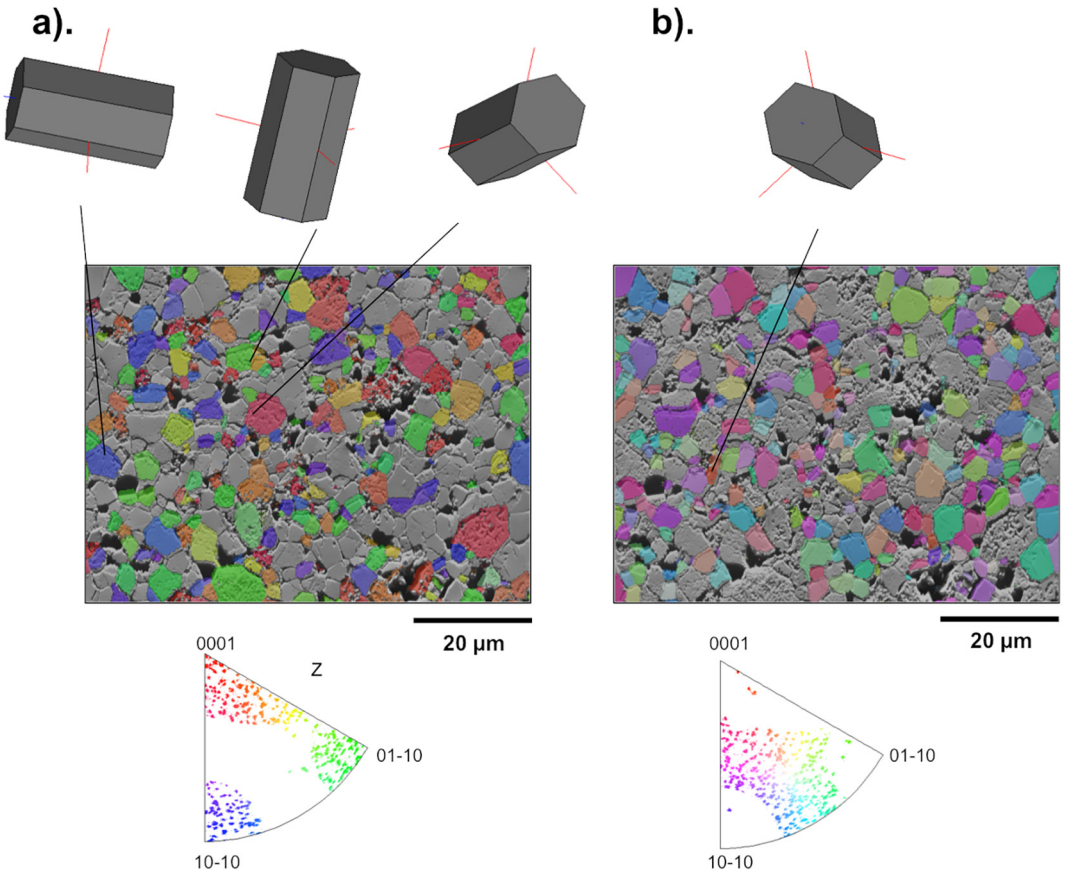

Fig. 5. High Mg-doped β-TCP acid-etched for 5 h in total: overlay of SEM images and crystal orientation maps derived from EBSD and displayed in Inverse Pole Figure (IPF) coloring (the reference direction is Z, i.e. the normal direction to the map): (a) etched grains and corresponding IPF (b) non-etched grains and corresponding IPF. For (a) and (b), examples of related 3D crystal orientation are shown on top of the figure. For Miller-Bravais indices of the 3D crystal representations, refer to Fig. 7.

both contained more Mg than anticipated from the synthesis protocol. Indeed, magnesium is a typical impurity of calcium phosphate minerals. Therefore, Mg is commonly found in reagents and in CaP materials prepared by solid-state synthesis. The low Mg-doped powder, although synthesized without adding any Mg to the high purity grade raw powders, was not completely Mg-free: it contained above 2000 ppm of Mg (Table 1). Assuming that all Mg atoms substituted Ca ones in the β-TCP lattice, this would correspond to a Mg to (Ca + Mg) ratio of 1 mol%. Likewise, although the synthesis protocol of the high Mg-doped powder aimed at substituting 5.6% of total calcium by magnesium ions, the powder contained around 13000 ppm (Table 1), corresponding to a 5.9 mol% ratio.

To obtain highly pure β-TCP samples, it was necessary to precipitate a Mg-free CDHA powder in the lab. Modifying the synthesis protocol permitted to reach a content in magnesium below the limit of quantification (Table 1). Finally, three β-TCP powders were synthesized. They contained around 0, 1 and 6 mol% Mg respectively, enabling to study the influence of magnesium on the resorption behavior of β-TCP samples.

After sintering, dense β-TCP disks (apparent density >90%) were obtained from the three powders and further characterized. The significant decrease in the lattice parameters with an increase in Mg content confirmed the doping of β-TCP with magnesium ions (Table 2). The substitution of Ca^{2+} by Mg^{2+} ions (having smaller radii than Ca^{2+}) in the β-TCP lattice is indeed known to induce a decrease in the unit cell parameters of β-TCP [22,31,44–47].

With the conditions used for EBSD mapping, no correlation seemed to exist between orientation of the exposed crystal planes and grain sizes, as might be expected given the rhombohedral nature of the β-TCP crystal. This was also consistent with the fact that Mg-doping decreased the lattice parameters but did not significantly alter the grain size of β-TCP samples (Table 3).

To simulate the resorption environment of CaP materials underneath osteoclast cells, dense samples were immersed in $NaHCO_3$-HCl solutions of pH 4.4. Indeed, osteoclasts degrade the inorganic components of bones by locally lowering the pH (as low as 3.9–4.5 [2,5,48]), leading to the dissolution of calcium phosphate crystals. The electrochemical equilibrium of the cells is maintained by ions exchange, among which H^+, Na^+, HCO_3^- and Cl^- ions [12,49,50], such as those composing the acidic solution used in this work. Partial dissolution of the polycrystalline bulk samples occurred, as already reported as a result of the culture of osteoclasts on CaP samples (*in vitro* [9,51] and *in vivo* [52]). Some grains appeared to remain intact, whereas the grain boundaries seemed to be highly dissolved. Etched grains presented very distinctive features of multiple spike-like intra-crystalline structures (Fig. 2a). Fig. 2b shows that such pillar-structures and an extensive dissolution of grain boundaries were also imaged at the surface of β-TCP samples after resorption by osteoclast cells. Likewise, these very distinctive spike-like features were described at the surface of β-TCP after cell-mediated resorption in several other works [2,3,8,12,51] and at the surface of hydroxyapatite samples [53]. In all cases, the observed pillar-structures seemed to exhibit constant diameters and to be regularly spaced (Fig. 2). Interestingly, the immersion of β-TCP samples in the acidic solution allowed to obtain comparable results to cell-mediated resorption, in terms of patterns topology and of crystallographic directions of the resulting intra-crystalline pillars

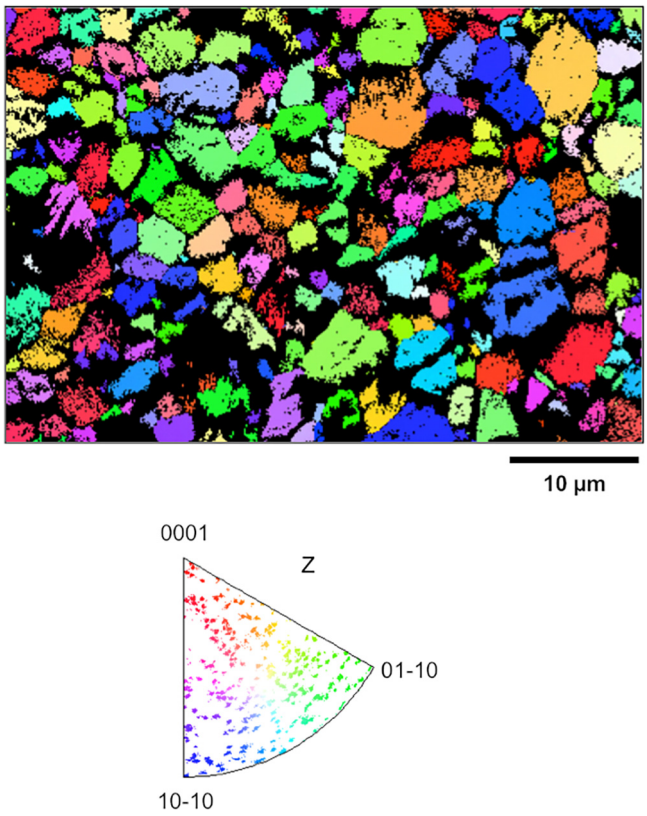

Fig. 6. Pure β-TCP after 24 h of contact with osteoclast cells (RANKL concentration = 5 ng/mL): overlay of a SEM image and crystal orientation maps derived from EBSD and displayed in Inverse Pole Figure (IPF) coloring (the reference direction is Z, i.e. the normal direction to the map).

(Fig. 7). In acidic dissolution (Fig. 7a) as well as in osteoclastic resorption (Fig. 7b), all pillars formed in a specific grain were aligned parallel to each other and in a direction correlated with the *c*-axis of the crystal. Additionally, Mg-doping had also similar consequences (grains etched less deeply and slower) in acidic dissolution and in osteoclastic resorption (Fig. 2).

Similar dissolution experiments, at acidic pH, have been conducted in different studies [1,12–14]. For instance, Matsunaga *et al.* observed the formation of comparable spike-like intra-crystalline structures when osteoclast cells were cultured on β-TCP samples, but they could not reproduce their formation during dissolution experiments in HCl solution at pH 2 [12]. SEM images performed at the surface of a pure β-TCP sample after 1 h immersion in a HCl solution of pH 2.5 (supplementary data, Fig. S4-b) led to the exact same observations as those reported by Matsunaga *et al.* [12]: grain boundaries were completely dissolved, but no spike-like structures were noticed. When the pH of the HCl solution was increased to 4.4, but still without any $NaHCO_3$ (supplementary data, Fig. S2-c), the sample retrieved from the solution did not show any sign of dissolution at all: the surface seemed similar to the polished surface of the initial samples, before acid etching. Finally, it was only when $NaHCO_3$ was added inside the HCl solution (as detailed in Materials and Methods section), that the intra-crystalline pillars were observed (supplementary data, Fig. S2-a). Thus, etching β-TCP samples in the $NaHCO_3$ – HCl solution may appear as a simple protocol to further study the mechanisms responsible for the formation of such regular intra-crystalline pillars. It is worth noting that, probably due to the slight acidification of the cell-culture medium with 15 mM HCl, a weak and homogeneous dissolution of the whole surface was experienced in cell-free control assays (supplementary data, Fig. S2-a). The characteristic pillars existed only after contact with cells, in extensively resorbed areas within the trails left by the cells (supplementary data, Fig. S2-b). However, care should be exercised when comparing results obtained in the frame of acellular tests with osteoclastic-resorption assays. In particular, adhesion, motion and proliferation of cells are disregarded in acellular tests: the acidic solution can only help to investigate physico-chemical dissolution processes occurring inside the tight resorption areas below adherent osteoclasts. Moreover, the exact micro-environment found underneath active osteoclasts, such as gradients in pH [5], is difficult to reproduce when immersing a material in a solution. When it comes to further extrapolate the resorption behavior of materials tested in *in-vitro* conditions to *in-vivo* assays, caution should be exercised even more. Indeed, the environment is far more complex *in-vivo*, with the presence of other cells, such as macrophages, of biological molecules, of proteins and of other ionic species. Their possible surface adsorption and interactions with bone graft substitutes are some of the critical parameters, which are disregarded in *in-vitro* assays.

However, results obtained in this study still permit to shed some light on the resorption mechanisms of pure and Mg-doped β-TCP materials. During immersion in the acidic solution, the dissolution of low Mg-doped β-TCP samples progressed both heterogeneously and anisotropically: some grains were etched nearly instantly (nearly one third of the surface after only 5 min, Fig. 1b), but only on a very thin surface layer. Then, the grains, which had already started to dissolve, were increasingly etched with immersion time, whereas others appeared to remain intact (Fig. 1a). Similar observations were made with non-doped and high Mg-doped samples, in which some grains were also preferentially etched (Figs. 1a, 2a). Interestingly, Seo *et al.* reported the same observations when they dipped dense hydroxyapatite samples in acidic solution (pH = 3) [13]. They showed by AFM that some specific grains undergo a significantly higher increase in roughness than others. Thus, the dissolution mechanisms depicted here for non-doped and Mg-doped β-TCP samples may well be generalizable to other resorbable CaP materials.

For all conditions investigated in this study, the Mg-doping slowed down both the acid-etching and the cell-mediated resorption of β-TCP samples (Figs. 1 and 2). This was again consistent with previous studies, which have widely reported that, whatever the experimental conditions, the substitution of calcium ions by magnesium ions decreases the solubility of the β-TCP phase [1,22,30,31]. Interestingly, the results reported here highlight that this solubility decrease arose from two different synergistic phenomena: i) a lower percentage of etched grains at a given time point (resulting in a lower etched area (Fig. 1b)) and ii) a lower dissolution rate of the grains, which were prone to dissolution (Fig. 1a): the grains, which were etched after 1 h, were etched deeper in non-doped than in low Mg-doped than in high Mg-doped samples (Figs. 1a, 2a). Because of this slow dissolution, it was hard to discriminate between etched and non-etched grains in high Mg-doped samples for short immersion durations. Thus, the percentage of etched surface could not be evaluated before 30 min (Fig. 1b).

Regarding the characterization of etched samples, the EBSD technique appeared to be complementary to XRD, since it enabled a local crystallographic analysis in SEM. Indeed, EBSD provides crystallographic orientation maps for a statistically significant number of grains. Mapping β-TCP samples revealed how crystal orientation of the grains had a strong influence on their dissolution behavior. In addition, the change of the crystal cell of β-TCP due to doping (Table 2) affected the crystal orientations susceptible to dissolution. In non-doped samples, all grains with the *c*-axis normal to the surface were acid-etched after 1 h, whereas some of the grains oriented in all other directions (i.e., *c*-axis nearly

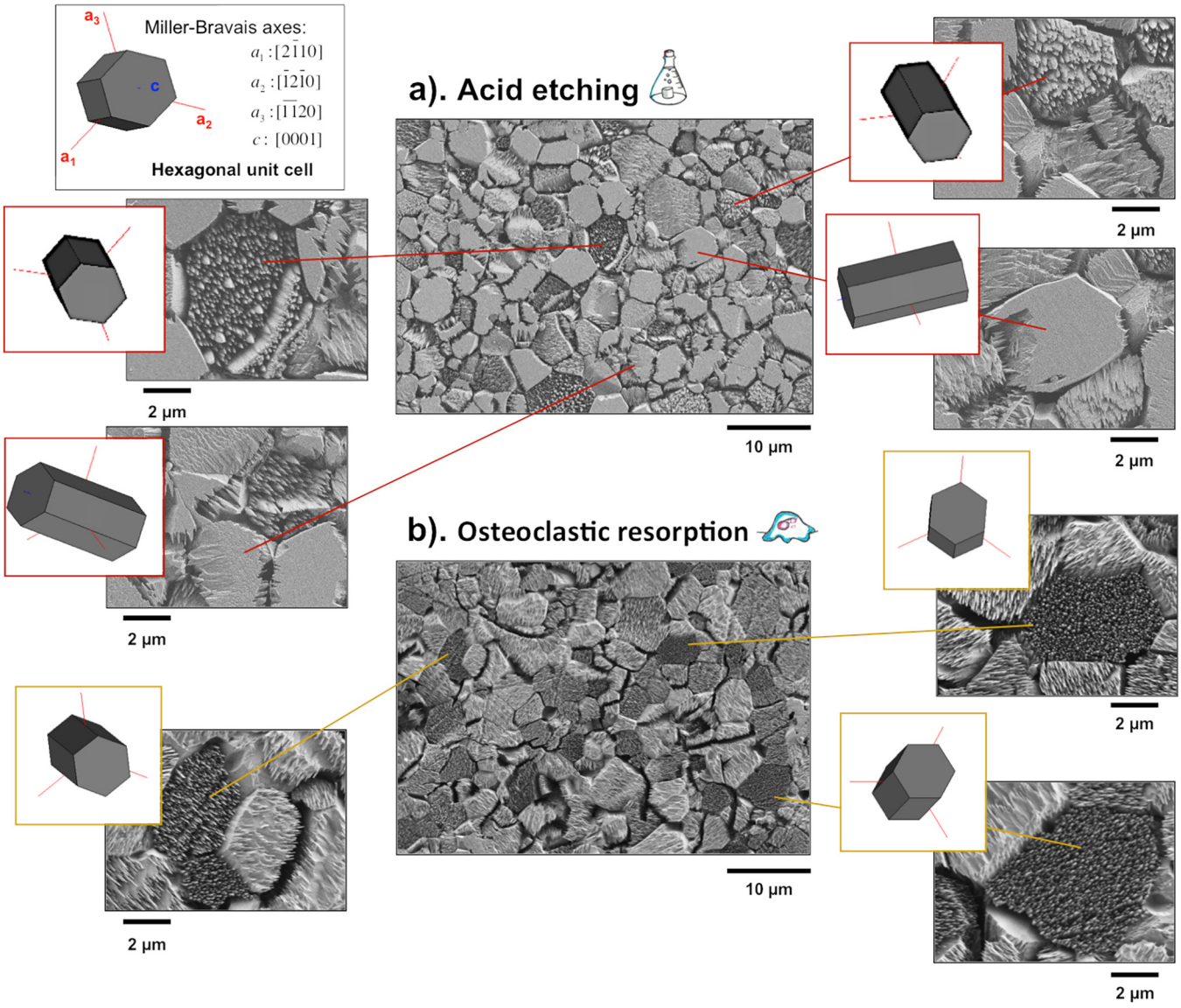

Fig. 7. SEM images of **pure β-TCP** samples (a) acid-etched for 1 h: observation of both non-etched and etched grains with characteristic intra-crystalline pillars (b) after 24 h of contact with osteoclast cells (RANKL concentration = 5 ng/mL): illustration of an area, where all grains are resorbed. (Insert, top left) Labelling of Miller-Bravais indices of the 3D crystal representations. (Inserts, side) Micrographs at high magnification highlighting the correlation between the orientation of the intra-crystalline pillars and the 3D crystal orientation of the grains.

parallel to the surface) were still intact (Fig. 3b): grains oriented with the *c*-axis in the *Z* direction tended to be more prone to dissolution than the others. It should be noted that this finding is consistent with the work by Tao *et al.* [54], who reported a preferred dissolution direction along the *c*-axis for nano-sized β-TCP monocrystals. However, they studied singular monocrystals of a few hundreds of nanometers, synthesized in very specific conditions (precipitation in an organic solvent), and composed of a hydrogen-rich calcium-deficient β–TCP phase rather than of pure β-TCP [55].

In low Mg-doped samples, only the grains with *c*-axis [0 0 0 1] nearly normal to the surface were preferentially etched (Fig. 4), while in high Mg-doped samples, any grain with a simple axis (*a*, *b* or *c*) normal to the surface was more prone to dissolution than the others (Figs. S3 and Fig. 5).

In non-doped and high Mg-doped samples, a slight difference was measured between the lattice parameters before etching and after etching (Table 2). On the contrary, the *c*-parameter of low Mg-doped samples significantly decreased during immersion in the acidic solution (Table 2). This result may arise from the low Mg content (Table 1): as grains containing Mg dissolve slower than grains without any Mg (Fig. 1), after 1 h etching, the non-etched grains may contain more Mg on average than the etched grains. Therefore, the mean *c*-parameter decreased at the surface of the low Mg-doped samples. This effect might even be reinforced by the fact that the first low Mg-doped grains to be etched were oriented with their *c*-axis normal to the sample's surface (Fig. 4), possibly explaining why the decrease of the cell parameter was measured for the *c*-parameter only (Table 2).

While in non-doped samples, etched grains happened to be slightly smaller than non-etched ones (Table 3), the contrary was observed for both low Mg-doped and high Mg-doped and for all immersion durations (Table 3). Given that no correlation was clearly evidenced between crystal orientation and grain size, it may indicate an effect of the size of a grain on its predisposition to dissolution. This would contradict results reported by Seo

et al., who did not find any significant difference for dissolved and non-dissolved grain sizes in the case of hydroxyapatite [13]. Nevertheless, it could explain why some of the grains oriented along the preferred orientations for dissolution were not etched. For instance, in high Mg-doped β-TCP, many grains with *a*, *b* or *c*-axis normal to the surface were not etched yet after 1 h (Fig. S3) and some were still intact after 5 h (Fig. 5b). Noteworthy, no other distinction could be found between etched and non-etched grains.

To sum up, the insertion of Mg into the β-TCP lattice stabilized the β-TCP phase against dissolution. At early stage of dissolution, only the grains oriented in the preferred dissolution direction were etched (along the *c*-axis for the non-doped β-TCP phase). Increasing the duration of immersion had two consequences: etched grains were etched deeper and deeper (Fig. 1a), while more grains started to dissolve (Fig. 1b). At later stage, grains of all orientations were finally etched (Fig. 3a). Thus, after 1 h etching, etched grains did not show any specific orientation in non-doped samples (Fig. 3a), whereas, due to a slower dissolution, only the grains with their *c*-axis nearly normal to the surface were etched in low Mg-doped samples (Fig. 4a). As in extensively resorbed areas after osteoclastic resorption (supplementary data, Fig. S2-b), all grains were etched, regardless of their crystal orientation (Fig. 6), it may be inferred that 24 h contact between osteoclasts and sample surfaces left enough time for the non-migrating osteoclasts to resorb all grains beneath them. This would then correspond to a longer etching duration in the simulated acellular acidic solution. In addition, the alignment of the intra-crystalline pillars formed at the surface of both etched and resorbed grains (Fig. 2) was correlated with the preferential direction for dissolution, i.e., the *c*-direction of the crystals (Fig. 7). When the Mg-doping was increased, the lattice parameters decreased (Table 2). This seemed to have a reinforcing effect on the [0 0 0 1] direction, at least in the high Mg-doped samples. Thus, the resorption of high Mg-doped samples was slower (Figs. 1 and 2), and all simple axes (*a*, *b* or *c*) became equivalent in terms of susceptibility to be dissolved (Fig. S3 and Fig. 5).

Last, these findings open new approaches to design materials with customized resorbability. One strategy could be to tune the crystal structure of CaP phases, either by incorporating single dopants or synergistic co-dopants [26,56–58] or by innovative synthesis routes [54,55]. Another strategy could be to texture samples in specific crystal orientations and thus combine optimal mechanical properties with appropriate resorption kinetics [59,60].

5. Conclusion

Dissolution of β-tricalcium phosphate samples was monitored in acidic solutions and compared to osteoclastic-mediated resorption. Acidic etching conditions used in this work proved to be a relevant and simple chemical alternative to cell-mediated resorption for the study of the mechanisms involved in the resorption of β-TCP bone graft substitutes. Doping β-TCP with Mg ions decreased its solubility: both the acid-etching and the cell resorption process were slowed down.

Electron backscatter diffraction was successfully used to map the crystallographic orientation of several thousand grains of polycrystalline β-TCP bulk samples and to study the correlation between grain orientation and resorption. For the three investigated compositions (non-doped, low Mg-doped and high Mg-doped samples), the early-stage dissolution was guided by grain orientation: some grains were preferentially etched, whereas others remained intact for hours, resulting in a rougher surface. Both acid-etched grains and grains resorbed by cells activity developed characteristic spike-like sub-structures, aligned parallel to each other within a same grain. Their alignment direction was correlated with the preferential direction for dissolution, i.e., the crystal direction [0 0 0 1] for pure β-TCP. Based on these results, it may be inferred that any change in the crystal parameters of a β-TCP material has a significant impact on its resorption process. Thus, doping β-TCP phases by ions of biological interest, such as Mg, Sr, Cu or Fe must influence not only the cellular response, but also the mechanism and kinetics of resorption of the material itself. These important findings pave the way for the design of bone graft substitutes with tailored resorption kinetics.

Acknowledgments

The authors would like to acknowledge Mirja Olsson for the synthesis of the powders, Nazim Boucida and Florian Mercier for their technical helps. This work was partly supported by the European Commission funding of the 7th Framework Program (Marie Curie Initial Training Networks; grant number: 289958, Bioceramics for bone repair). This study was partly supported by the Swiss National Science Foundation (SNSF; 200021_169027).

Appendix A. Supplementary data

Supplementary data to this article can be found online at https://doi.org/10.1016/j.actbio.2019.02.045.

References

[1] A. Ito, Y. Sogo, A. Yamazaki, M. Aizawa, A. Osaka, S. Hayakawa, M. Kikuchi, K. Yamashita, Y. Tanaka, M. Tadokoro, L.A. de Sena, F. Buchanan, H. Ohgushi, M. Bohner, Interlaboratory studies on in vitro test methods for estimating in vivo resorption of calcium phosphate ceramics, Acta Biomater. 25 (2015) 347–355.
[2] M. Bohner, L. Galea, N. Doebelin, Calcium phosphate bone graft substitutes: failures and hopes, J. Eur. Ceram. Soc. 32 (11) (2012) 2663–2671.
[3] R. Detsch, A.R. Boccaccini, The role of osteoclasts in bone tissue engineering, J. Tissue Eng. Regen. Med. (2014).
[4] K. Väänänen, Mechanism of osteoclast mediated bone resorption—rationale for the design of new therapeutics, Adv. Drug Deliv. Rev. 57 (2005) 959–971.
[5] I.A. Silver, R.J. Murrills, D.J. Etherington, Microelectrode studies on the acid microenvironment beneath adherent macrophages and osteoclasts, Exp. Cell Res. 175 (2) (1988) 266–276.
[6] D.O. Costa, P.D.H. Prowse, T. Chrones, S.M. Sims, D.W. Hamilton, A.S. Rizkalla, S. J. Dixon, The differential regulation of osteoblast and osteoclast activity by surface topography of hydroxyapatite coatings, Biomaterials 34 (30) (2013) 7215–7226.
[7] N.L. Davison, B. ten Harkel, T. Schoenmaker, X. Luo, H. Yuan, V. Everts, F. Barrère-de Groot, J.D. de, Bruijn, "Osteoclast resorption of beta-tricalcium phosphate controlled by surface architecture", Biomaterials 35 (26) (2014) 7441–7451.
[8] S.A. Redey, S. Razzouk, C. Rey, D. Bernache-Assollant, G. Leroy, M. Nardin, G. Cournot, Osteoclast adhesion and activity on synthetic hydroxyapatite, carbonated hydroxyapatite, and natural calcium carbonate: relationship to surface energies, J. Biomed. Mater. Res. 45 (1999) 140–147.
[9] R. Detsch, D. Hagmeyer, M. Neumann, S. Schaefer, A. Vortkamp, M. Wuelling, G. Ziegler, M. Epple, The resorption of nanocrystalline calcium phosphates by osteoclast-like cells, Acta Biomater. 6 (2010) 3223–3233.
[10] R.J. Egli, S. Gruenenfelder, N. Doebelin, W. Hofstetter, R. Luginbuehl, M. Bohner, Thermal treatments of calcium phosphate biomaterials to tune the physico-chemical properties and modify the in vitro osteoclast response, Adv. Eng. Mater. 13 (3) (2011) B102–B107.
[11] V.M. Wu, V. Uskoković, Is there a relationship between solubility and resorbability of different calcium phosphate phases in vitro?, Biochim Biophys. Acta - Gen. Subj. 1860 (10) (2016) 2157–2168.
[12] A. Matsunaga, M. Takami, T. Irié, K. Mishima, K. Inagaki, R. Kamijo, Microscopic study on resorption of β-tricalcium phosphate materials by osteoclasts, Cytotechnology 67 (4) (2015) 727–732.
[13] D.S. Seo, J.K. Lee, AFM analysis of anisotropic dissolution in dense hydroxyapatite, Ultramicroscopy 108 (10) (2008) 1157–1162.
[14] M. Gallo, S. Tadier, S. Meille, J. Chevalier, Resorption of calcium phosphate materials: considerations on the in vitro evaluation, J. Eur. Ceram. Soc. 38 (3) (2018) 899–914.
[15] M.E. Smith, K.G. Knauss, S.R. Higgins, Effects of crystal orientation on the dissolution of calcite by chemical and microscopic analysis, Chem. Geol. 360–361 (2013) 10–21.
[16] L. Wang, G.H. Nancollas, Calcium orthophosphates: crystallization and dissolution, Chem. Rev. 108 (11) (Nov. 2008) 4628–4669.

[17] L. Wang, R. Tang, T. Bonstein, C.A. Orme, P.J. Bush, G.H. Nancollas, A new model for nanoscale enamel dissolution, J. Phys. Chem. B 109 (2) (Jan. 2005) 999–1005.
[18] M. Bohner, Calcium orthophosphates in medicine: from ceramics to calcium phosphate cements, Injury 31 (2000) D37–D47.
[19] L. Gremillard, S. Meille, J. Chevalier, J. Zhao, V. Fridrici, P. Kapsa, J. Geringer, J. Uribe, Degradation of Bioceramics, Springer, 2012.
[20] H.-S.Y. Ryu Hyuk-Joon, Kug Sun Hong, Bong-Sun Chang, Choon-Ki Lee, Sung-Soo Chung, An improvement in sintering property of b-tricalcium phosphate by addition of calcium pyrophosphate, Biomaterials 23 (2002) 909–914.
[21] M. Bohner, Bioresorbable Ceramics, Woodhead publishing in Materials, Boston, 2008.
[22] X. Li, A. Ito, Y. Sogo, X. Wang, R.Z. LeGeros, Solubility of Mg-containing β-tricalcium phosphate at 25°C, Acta Biomater. 5 (1) (2009) 508–517.
[23] M.S. Yashima Atsushi, Takashi Kamiyama, Akinori Hoshikawa, Crystal structure analysis of β-tricalcium phosphate $Ca_3(PO_4)_2$ by neutron powder diffraction", J. Solid State Chem. 175 (2) (2003) 272–277.
[24] Y. Ando, Phase Diagrams of $Ca_3(PO_4)_2$-$Mg_3(PO_4)_2$ and $Ca_3(PO_4)_2$-$CaNaPO_4$ Systems, Bull. Chem. Soc. Jpn. 31 (2) (1958) 201–205.
[25] Z. Seeley, A. Bandyopadhyay, S. Bose, Tricalcium phosphate based resorbable ceramics: influence of NaF and CaO addition, Mater. Sci. Eng., C 28 (1) (2008) 11–17.
[26] W. Xue, K. Dahlquist, A. Banerjee, A. Bandyopadhyay, S. Bose, Synthesis and characterization of tricalcium phosphate with Zn and Mg based dopants, J. Mater. Sci. - Mater. Med. 19 (7) (2008) 2669–2677.
[27] M. Olsson, Chemical stability of grain boundaries in b-tricalcium phosphate ceramics, Master Thesis, no. ISSN: 1650-8297, UPTEC-K12 002, 2012.
[28] R.K. Singh, M. Srivastava, N.K. Prasad, S. Awasthi, A. Dhayalan, S. Kannan, Iron doped β-Tricalcium phosphate: synthesis, characterization, hyperthermia effect, biocompatibility and mechanical evaluation, Mater. Sci. Eng., C 78 (2017) 715–726.
[29] R. Famery, N. Richard, P. Boch, Preparation of α- and β-tricalcium phosphate ceramics, with and without magnesium addition, Ceram. Int. 20 (5) (1994) 327–336.
[30] R.M.H. Verbeeck, P.A.M. De Bruyne, F.C.M. Driessens, R.A. Terpstra, F. Verbeek, Solubility behavior of Mg-containing β-$Ca_3(PO_4)_2$, Bull. Soc. Chim. Belg. 95 (1986) 455–476.
[31] C. Tardei, F. Grigore, I. Pasuk, S. Stoleriu, The study of Mg^{2+}/Ca^{2+} substitution of β-tricalcium phosphate, J. Optoelectron. Adv. Mater. 8 (2006).
[32] T.-W. Kim, H.-S. Lee, D.-H. Kim, H.-H. Jin, K.-H. Hwang, J.K. Lee, H.-C. Park, S.-Y. Yoon, In situ synthesis of magnesium-substituted biphasic calcium phosphate and in vitro biodegradation, Mater. Res. Bull. 47 (9) (2012) 2506–2512.
[33] A. Hoppe, N.S. Güldal, A.R. Boccaccini, A review of the biological response to ionic dissolution products from bioactive glasses and glass-ceramics, Biomaterials 32 (2011) 2757–2774.
[34] S. Castiglioni, A. Cazzaniga, W. Albisetti, J.A.M. Maier, Magnesium and osteoporosis: current state of knowledge and future research directions, Nutrients 5 (8) (2013) 3022–3033.
[35] A. Destainville, E. Champion, D. Bernache-Assollant, E. Laborde, Synthesis, characterization and thermal behavior of apatetic tricalcium phosphate, Mater. Chem. Phys. 80 (1) (2003) 269–277.
[36] M. Descamps, O. Richart, P. Hardouin, J.C. Hornez, A. Leriche, Synthesis of macroporous β-tricalcium phosphate with controlled porous architectural, Ceram. Int. 34 (5) (2008) 1131–1137.
[37] W. Xie, S. Lorenz, S. Dolder, W. Hofstetter, Extracellular iron is a modulator of the differentiation of osteoclast lineage cells, Calcif. Tissue Int. 98 (3) (2016) 275–283.
[38] N. Ruef, S. Dolder, D. Aeberli, M. Seitz, D. Balani, W. Hofstetter, Granulocyte-macrophage colony-stimulating factor-dependent CD11c-positive cells differentiate into active osteoclasts, Bone 97 (2017) 267–277.
[39] J. Choy, C.E. Albers, K.A. Siebenrock, S. Dolder, W. Hofstetter, F.M. Klenke, Incorporation of RANKL promotes osteoclast formation and osteoclast activity on β-TCP ceramics, Bone 69 (2014) 80–88.
[40] S. Dolder, W. Hofstetter, A. Wetterwald, R.C. Mühlbauer, R. Felix, Effect of monoterpenes on the formation and activation of osteoclasts in vitro, J. Bone Miner. Res. 21 (4) (2009) 647–655.
[41] G. Albano, S. Dolder, M. Siegrist, A. Mercier-Zuber, M. Auberson, C. Stoudmann, W. Hofstetter, O. Bonny, D.G. Fuster, Increased bone resorption by osteoclast-specific deletion of the sodium/calcium exchanger isoform 1 (NCX1), Pflügers Arch. - Eur. J. Physiol. 469 (2) (2017) 225–233.
[42] R. Balga, A. Wetterwald, J. Portenier, S. Dolder, C. Mueller, W. Hofstetter, Tumor necrosis factor-alpha: alternative role as an inhibitor of osteoclast formation in vitro, Bone 39 (2) (2006) 325–335.
[43] Available on: <Http://imagej.nih.gov/ij/>, NIH National Institute of Health, Image J.
[44] R. Enderle, F. Götz-Neunhoeffer, M. Göbbels, F.A. Müller, P. Greil, Influence of magnesium doping on the phase transformation temperature of β-TCP ceramics examined by Rietveld refinement, Biomaterials 26 (17) (2005) 3379–3384.
[45] S. Kannan, F. Goetz-Neunhoeffer, J. Neubauer, J.M.F. Ferreira, Ionic substitutions in biphasic hydroxyapatite and beta TCP mixtures, structural analysis by Rietveld refinement, J. Am. Ceram. Soc. 91 (2008) 1–12.
[46] M. Frasnelli, V.M. Sglavo, Effect of Mg2+ doping on beta–alpha phase transition in tricalcium phosphate (TCP) bioceramics, Acta Biomater. 33 (2016) 283–289.
[47] I. Cacciotti, A. Bianco, High thermally stable Mg-substituted tricalcium phosphate via precipitation, Ceram. Int. 37 (1) (2011) 127–137.
[48] P. Frayssinet, N. Rouquet, F. Tourenne, J. Fages, D. Hardy, G. Bonel, Cell-degradation of calcium phosphate ceramics, Cells Mater. 3 (6) (1993).
[49] A. Gomez-Brouchet, REMODELAGE OSSEUX: ASPECTS BIOLOGIQUES ET MOLECULAIRES, Serv. d'Anatomie Cytol. Pathol. CHU Rangueil, Toulouse.
[50] J. Nolan, Fluid replacement, Br. Med. Bull. 55 (4) (1999) 821–843.
[51] R. Detsch, H. Mayr, G. Ziegler, Formation of osteoclast-like cells on HA and TCP ceramics, Acta Biomater. 4 (1) (2008) 139–148.
[52] S. Yamada, D. Heymann, J.-M. Bouler, G. Daculsi, Osteoclastic resorption of calcium phosphate ceramics with different hydroxyapatite/beta-tricalcium phosphate ratios, Biomaterials 18 (1997) 1037–1041.
[53] J.D. de Bruijn, Y.P. Bovell, J.E. Davies, C.A. van Blitterswijk, Osteoclastic resorption of calcium phosphates is potentiated in postosteogenic culture conditions, J. Biomed. Mater. Res. (1994).
[54] J. Tao, W. Jiang, H. Zhai, H. Pan, X. Xu, R. Tang, Structural components and anisotropic dissolution behaviors in one hexagonal single crystal of β-tricalcium phosphate, Cryst. Growth Des. 8 (7) (Jul. 2008) 2227–2234.
[55] C. Stähli, J. Thüring, L. Galea, S. Tadier, M. Bohner, N. Döbelin, Hydrogen-substituted β-tricalcium phosphate synthesized in organic media, Acta Crystallogr. Sect. B 72 (6) (2016) 875–884.
[56] S.S. Banerjee, S. Tarafder, N.M. Davies, A. Bandyopadhyay, S. Bose, Understanding the influence of MgO and SrO binary doping on the mechanical and biological properties of β-TCP ceramics, Acta Biomater. 6 (10) (2010) 4167–4174.
[57] I.H. García-Páez, R.G. Carrodeguas, A.H. De Aza, C. Baudín, P. Pena, Effect of Mg and Si co-substitution on microstructure and strength of tricalcium phosphate ceramics, J. Mech. Behav. Biomed. Mater. 30 (2014) 1–15.
[58] D. Bellucci, A. Sola, I. Cacciotti, C. Bartoli, M. Gazzarri, A. Bianco, F. Chiellini, V. Cannillo, Mg- and/or Sr-doped tricalcium phosphate/bioactive glass composites: synthesis, microstructure and biological responsiveness, Mater. Sci. Eng., C 42 (2014) 312–324.
[59] L. Galea, D. Alexeev, M. Bohner, N. Doebelin, A.R. Studart, C.G. Aneziris, T. Graule, Textured and hierarchically structured calcium phosphate ceramic blocks through hydrothermal treatment, Biomaterials 67 (2015) 93–103.
[60] S. Chamary, D. Hautcoeur, J.-C. Hornez, A. Leriche, F. Cambier, Bio-inspired hydroxyapatite dual core-shell structure for bone substitutes, J. Eur. Ceram. Soc. 37 (16) (2017) 5321–5327.